IEEE Access
Multidisciplinary ⋮ Rapid Review ⋮ Open Access Journal

Received 19 January 2024, accepted 8 February 2024, date of publication 12 February 2024, date of current version 26 February 2024.

Digital Object Identifier 10.1109/ACCESS.2024.3365141

METHODS

Residual Stress and Distortion Prediction for Laser Directed Energy Deposition Based on Cyclic Heat Transfer Model

YUANXIN CHAI[1], DIANQI LI[1], LIGUO MIAO[1], JINGHU TANG[2], AND FEI XING[3]
[1]School of Mechanical Engineering, Shenyang University of Technology, Shenyang 110870, China
[2]School of Mechanical Engineering and Automation, Northeastern University, Shenyang 110819, China
[3]Nanjing Zhongke Raycham Laser Technology Company Ltd., Nanjing 210038, China

Corresponding author: Yuanxin Chai (chaiyuanxin@smail.sut.edu.cn)

This work was supported by the National Key Research and Development Program of China under Grant 2022YFB4602200.

ABSTRACT Predicting the residual stress and distortion caused by inhomogeneous temperature fields in the laser directed energy deposition (LDED) process is a challenging task. This study proposes a novel thermodynamic coupling simulation method based on the cyclic heat transfer model to accurately predict temperature, stress, and distortion evolution during the deposition process. The model effectively calculates the layer-by-layer superposition of thermal effects and cyclic accumulation of thermal stress during the deposition process, leading to improved prediction accuracy for temperature, residual stress, and distortion. Initially, the heat source model, the cyclic heat transfer model, and the thermoelastic matrix are established. The thermoelastic constitutive equation and the equilibrium differential equation are formulated to capture the actual process characteristics of the LDED accurately in order to achieve the thermodynamic coupling solution. Then, numerical simulations are performed on a typical model specimen, with simulation parameters consistent with the actual deposition parameters. Finally, the predicted results are validated through actual deposition experiments, and the temperature, stress, and distortion history are analyzed. The results demonstrate that the cyclic thermodynamic coupling model proposed in this study can effectively predict the deposited components' temperature, residual stress, and distortion evolution. This study establishes a crucial foundation for achieving precision and performance control in the deposition process and reducing residual stress and distortion in the components.

INDEX TERMS Laser directed energy deposition (LDED), cyclic heat transfer model, thermodynamic coupling, residual stress, distortion.

I. INTRODUCTION

Laser directed energy deposition (LDED) is an advanced manufacturing technology that integrates precision and performance demands. A high-energy laser beam is utilized to melt both the substrate (or deposited layers) and the coaxially injected powder, forming a molten pool. The melted powder is deposited in the molten pool area and forms the deposition layers after cooling and solidification. The deposition layers incrementally grow in a predetermined pattern through additive formation [1]. This technology possesses high flexibility and efficiency, reducing energy consumption and industrial costs. It has widespread applications in various fields, including nuclear power, aerospace, marine engineering, bioengineering, and medicine [2].

Nevertheless, the complex and alternating hot-cold cycles occurring during the deposition process contribute to the generation of thermal stress. Although a small portion of this stress is alleviated during the subsequent deposition process, the majority remains and transforms into residual stress. Residual stress can result in part distortion and, in severe cases, crack failure, which poses a critical challenge in

The associate editor coordinating the review of this manuscript and approving it for publication was Dominik Strzalka.

advancing the LDED technology. Consequently, the efficient and accurate prediction of residual stress and distortion is of utmost importance in enhancing the quality of the deposited parts [3], [4], [5]. The most direct method for evaluating residual stress and distortion is through expensive and time-consuming experimental measurements, which add to the overall production or research costs. A cost-effective alternative lies in numerical simulation, which can be applied during the design phase to quickly predict and assess these factors.

Numerical simulation studies of the LDED process, utilizing the finite element method, have been widely embraced by numerous scholars. Yushu et al. [6] introduced a novel thermodynamic model, free from geometry constraints, for predicting residual stress and distortion. Notably, the model eliminated the need for assumptions regarding the part's geometry and effectively captured geometric errors and surface roughness during the actual deposition process. Cooke et al. [7] proposed a thermodynamic coupled finite element model for the LDED process. This model accounted for the influence of phase transformation on latent heat and residual stress, allowing it to provide predictions for temperature, residual stress, distortion, and microstructure. Yang et al. [8] employed in-situ measurements and numerical simulations to study the distortion of the substrate during the deposition process. However, the experimental results exhibited a more pronounced fluctuation than the simulated results. This difference could be attributed to clamping errors during the actual process, which led to uneven heat distribution, residual stress, and distortion. These factors were not considered in the simulation. Pourabdollah et al. [9] developed a transient thermodynamic model to predict deposited hollow rectangular parts' temperature, stress, and distortion. The model utilized the layer clustering method, a commonly adopted approach to reduce computational time. Kiran et al. [10] developed a thermodynamic model for the LDED process of 316L stainless steel. However, the model had computational accuracy and efficiency limitations when using transient thermal inputs for simulation. Nain et al. [11] developed a three-dimensional transient finite element model with Quiet/Active element activation. An elongated ellipsoid heat source model was used to reduce the simulation time step by dividing the complete track into several sub-tracks. Solving each sub-track in one simulation time step reduced the finite element computation time.

All of the studies above showcase the efficacy of numerical simulation techniques in accurately modeling the evolution of temperature and stress fields during the LDED process and predicting the residual stress and distortion of deposited parts. However, these studies overlook the impact of cyclic thermodynamic effects on the deposition process. As a result, the simulation results cannot accurately depict the actual deposition process and exhibit notable disparities compared to experimental measurements. Given the cyclic thermodynamic coupling issue in the LDED process and the current state of research in this field, this study introduces a method for predicting residual stress and distortion based on the cyclic heat transfer model. The contribution of this study lies in developing a cyclic thermodynamic coupling model for predicting the temperature, residual stress, and distortion evolution of deposited parts based on the characteristics of cyclic thermodynamic effects in the LDED process. The model can effectively calculate the layer-by-layer superposition of thermal effects during the deposition process and the cyclic cumulative thermal stress. It enables tracking cyclic thermodynamic effects process data consistent with the actual process characteristics. Additionally, it allows for a comprehensive analysis of the thermodynamic behavior during the deposition process. This enhancement improves the accuracy of predicting temperature, residual stress, and distortion. Consequently, it reduces the number of experimental iterations required to optimize the deposition process to a significant extent. In this study, Inconel 718, a widely used alloy in engineering, was chosen as the material for simulations and experiments. The research methodology and conclusions can be expanded to other metallic materials, offering valuable reference values for predicting the thermodynamic outcomes of the LDED process.

The remainder of this manuscript is organized as follows: In Section II, the heat source model, cyclic heat transfer model, thermoelastic matrix, thermoelastic constitutive equation, and equilibrium differential equation are established for the thermodynamic coupling solution. Section III describes the selected powder materials for the study and the equipment and methods used to measure temperature, residual stress, and distortion. Section IV conducts thermodynamic coupling simulations using a typical specimen. The predicted results are verified by deposition experiments with the same process parameters, followed by an analysis of the evolution history of temperature, stress, and distortion during the deposition process. Finally, Section V summarizes the findings of this paper and proposes directions for further research.

II. MODEL DESCRIPTION

The procedure for the cyclic thermodynamic coupling simulation solution proposed in this study is illustrated in Fig. 1. Firstly, the laser heat source parameters are utilized to construct the equivalent thermal loading. Then, the total strain is obtained through the superposition of the cyclic heat transfer model. Next, the thermoelastic matrix is constructed. Based on the spatial problem of thermoelastic mechanics, the thermoelastic constitutive equation, geometry equation, and equilibrium differential equation are established. Finally, the

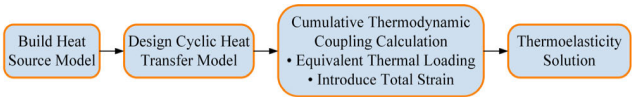

FIGURE 1. Cyclic thermodynamic coupling simulation solution procedure for the LDED process.

stress and strain are solved by substituting the equilibrium differential equation and the thermoelastic constitutive equation based on the provided equivalent thermal loading.

A. HEAT SOURCE MODEL

Based on the laser emission characteristics, the laser source is commonly modeled as a Gaussian heat source, with the maximum heat flux density exponentially decreasing from the center outwards [12]. The fundamental equation is described as follows:

$$q(r) = \frac{3\eta P}{\pi R^2} \exp\left(-\frac{3r^2}{R^2}\right) \tag{1}$$

where $q(r)$ is the laser heat flux density, R is the laser spot radius, η is the laser energy absorption rate, P is the laser power, and r is the distance from the calculation point to the center of the heat source.

As a result, the heat flux density of the laser heat source can be determined based on the provided laser power, spot size, and other parameters. The heat flux density model is depicted in Fig. 2, showcasing the highest heat flux density at the center. The heat transfer energy is maximized towards the surrounding area and gradually diminishes as it spreads outward in all directions.

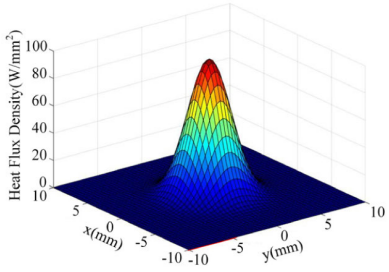

FIGURE 2. Schematic diagram of the heat flux density model.

B. CYCLIC HEAT TRANSFER MODEL

During the deposition process, the laser beam irradiates the metal powder, generating thermal energy that is stored and transferred to the surrounding area. When the high-energy laser beam comes into contact with the material, it creates a high-temperature molten pool, transferring the thermal energy to the substrate through thermal conduction. The high-temperature molten pool influences the surrounding air, inducing natural convection and facilitating convective heat transfer between the molten pool and the external environment. Simultaneously, the molten pool exchanges thermal energy with the surroundings through thermal radiation [13], [14].

1) THERMAL CONDUCTION

When the high-energy laser beam interacts with the substrate, the intense laser energy quickly transfers to the lower-temperature substrate, resulting in a vigorous energy exchange that facilitates the bonding of the deposited material to the substrate. The process of thermal conduction adheres to Fourier's law, and the basic equation can be described as follows [15], [16]:

$$q = -k\frac{\partial T}{\partial n} \tag{2}$$

where q is the heat flux density, k is the thermal conductivity, and $\frac{\partial T}{\partial n}$ is the temperature gradient.

2) THERMAL CONVECTION

During the deposition process, the air surrounding the molten pool undergoes expansion due to the high temperature. This expansion leads to the movement of heated gas away from the heat source, generating airflow. As the gas flow persists, convective heat transfer occurs [17], [18]. The calculation of convective heat transfer follows Newton's law of cooling:

$$q = h_c\,(T - T_0) \tag{3}$$

where q is the heat flux density, h_c is the convective heat transfer coefficient, T is the object boundary surface temperature, and T_0 is the surrounding ambient medium temperature.

3) THERMAL RADIATION

During the deposition process, a portion of the thermal energy is emitted to the surrounding environment through radiation [19], [20]. Thermal radiation is commonly governed by the Stefan-Boltzmann law:

$$q = \varphi\chi\left(T^4 - T_0^4\right) \tag{4}$$

where q is the heat flux density, φ is the emissivity, between 0 and 1, χ is the Stefan-Boltzmann constant, about 5.67×10^{-8} W/(m^2·K^4), T is the object boundary surface temperature, and T_0 is the surrounding ambient medium temperature.

4) ENERGY GENERATED IN SOLIDS

When the laser is activated, it generates heat in the powder exposed to the laser beam. The generated heat energy is determined by multiplying the heat flux density with the volume:

$$E_g = \dot{q}V \tag{5}$$

where E_g is the energy generated, $\dot{q}$ is the heat flux density, and V is the volume of the heated object.

5) ENERGY STORED IN SOLIDS

Metal powder generates thermal energy and increases in temperature with continued energy input. The thermal energy is stored in the solid material in proportion to the material's thermal coefficient.

$$E_s = \rho c V\frac{\partial T}{\partial t} \tag{6}$$

where E_s is the energy stored, ρ is the density of the material, and c is the specific heat of the material.

Thus, the heat transfer equation per unit volume is obtained as:

$$\rho c_p \frac{\partial T}{\partial t} = \nabla \left(-k \nabla T\right) \tag{7}$$

where c_p is the specific heat corresponding to the current temperature of the node material.

Based on this premise, the compound cyclic heat transfer equation can be derived by taking into account the cyclic heat transfer within the previously deposited layer:

$$\rho c_p \frac{\partial T}{\partial t} = \sum\nolimits_{i=1}^{n} \nabla_i \left(-k \Delta T_i\right) \tag{8}$$

where i represents the number of layers involved in heat transfer, determined by the temperature difference $\Delta \mathrm{T_i} < \theta$ between the layers, θ is a user-defined threshold value.

The moving laser heat source affects the state of the powder, leading to rapid melting and solidification. The thermal energy diffuses through the molten pool to the substrate, causing significant changes in the temperature of the molten pool over time. This creates a typical nonlinear transient heat transfer problem that satisfies Fourier's law of thermal conduction. Fourier's law can be expressed as follows:

$$\begin{aligned} \rho c \frac{\partial T}{\partial t} = &\frac{\partial}{\partial x}\left(k_x \frac{\partial T}{\partial x}\right) + \frac{\partial}{\partial y}\left(k_y \frac{\partial T}{\partial y}\right) \\ &+ \frac{\partial}{\partial z}\left(k_z \frac{\partial T}{\partial z}\right) + \dot{q} \end{aligned} \tag{9}$$

where k_x, k_y, k_z are the thermal conductivity in three directions.

If the thermal conductivity is the same in three directions X, Y, and Z, the material can be assumed to be isotropic, where $\mathrm{k_x} = \mathrm{k_y} = \mathrm{k_z} = \mathrm{k}$.

C. THERMODYNAMIC COUPLING ANALYSIS

Thermal strain is typically expressed as the product of the coefficient of thermal expansion and the temperature, as follows:

$$\varepsilon^{th} = \int_{T_{ref}}^{t} \alpha_e \left(T\right) dT \approx \alpha_e \Delta T \tag{10}$$

where α_e is the coefficient of thermal expansion corresponding to the temperature of the current node material, T_{ref} is the reference temperature of the previous layer.

During the elastic distortion phase, the total elastic distortion of the part includes the thermal expansion strain $\left\{\varepsilon^{th}\right\}$ and the strain $\left\{\varepsilon^{f}\right\}$ caused by the thermal stress constraint in the front deposition layer. This can be expressed as follows:

$$\left\{\varepsilon^{e}\right\} = \left\{\varepsilon^{f}\right\} + \left\{\varepsilon^{th}\right\} \tag{11}$$

As the temperature increases during the deposition process, the strain and stress of the material also increase. When the temperature reaches the transition limit from elastic to plastic, the material transforms from elastic to plastic distortion. The condition for elastoplastic transition is derived from the Mises yield criterion and can be expressed as follows:

$$C = \frac{1}{3}\sigma_s^2 \left(\sigma_1 = \sigma_s, \sigma_2 = \sigma_3 = 0\right) \tag{12}$$

where C is a constant related to the material properties but independent of the stress state, σ_1, σ_2, and σ_3 are the principal stress in the three orthogonal directions, and σ_s is the yield strength of the material.

When the material enters the plastic distortion phase, the constitutive equation is utilized to calculate the elastoplastic strain, which is based on the Prandtl-Reuss flow criterion.

$$\begin{aligned} d\varepsilon_{ii} &= \frac{1}{2G} d\sigma'_{ii} + d\lambda \sigma'_{ii}, d\varepsilon_{jj}, \ldots, d\varepsilon_{kk}, \ldots; \\ d\tau_{ij} &= \frac{1}{G} d\tau_{ij} + 2d\lambda \tau_{ij}, d\tau_{jk}, \ldots, d\tau_{ik}, \ldots; \\ &\quad (i, j, k = x, y, z) \end{aligned} \tag{13}$$

where $d\lambda$ is a positive transient constant.

Through layer-by-layer accumulation, the total strain is formed in each direction [21], [22], [23], [24]:

$$\left\{\varepsilon_{ij}\right\} = \left\{\varepsilon^{e}\right\} + \left\{\varepsilon^{p}\right\} = \left\{\varepsilon^{f}\right\} + \left\{\varepsilon^{th}\right\} + \left\{\varepsilon^{p}\right\} \tag{14}$$

where ε^e is the elastic strain and ε^p is the plastic strain.

The thermoelastic matrix for an orthotropic material can be obtained from the generalized Hooke's law:

$$\begin{aligned} \begin{Bmatrix} \varepsilon_x \\ \varepsilon_y \\ \varepsilon_z \\ \gamma_{xy} \\ \gamma_{yz} \\ \gamma_{zx} \end{Bmatrix} = &\begin{bmatrix} \frac{1}{E_x} & -\mu_{xy} & -\mu_{xz} & 0 & 0 & 0 \\ -\mu_{xy} & \frac{1}{E_y} & -\mu_{yz} & 0 & 0 & 0 \\ -\mu_{xz} & -\mu_{yz} & \frac{1}{E_z} & 0 & 0 & 0 \\ 0 & 0 & 0 & \frac{1}{G_{xy}} & 0 & 0 \\ 0 & 0 & 0 & 0 & \frac{1}{G_{yz}} & 0 \\ 0 & 0 & 0 & 0 & 0 & \frac{1}{G_{zx}} \end{bmatrix} \begin{Bmatrix} \sigma_x \\ \sigma_y \\ \sigma_z \\ \tau_{xy} \\ \tau_{yz} \\ \tau_{zx} \end{Bmatrix} \\ &+ \begin{Bmatrix} \alpha_{ex} \\ \alpha_{ey} \\ \alpha_{ez} \\ 0 \\ 0 \\ 0 \end{Bmatrix} T \end{aligned} \tag{15}$$

When the strain is known, the stress solution can be performed according to (15). If the material is determined to be in a state of plastic distortion based on (12), the elastoplastic increment value (13) can be added after (15).

When the material is assumed to be isotropic, $E_i = E$, $\mu_{ij} = \mu$, $\alpha_{ij} = \alpha$, it means that the material coefficients are the same in all directions. However, in this study, the thermodynamic coupling calculation ignored the differences in material anisotropy. Since there is a lack of literature data on the variation of material anisotropy coefficients with temperature, this study simplifies the treatment by assuming material isotropy.

D. THERMODYNAMIC COUPLING SOLUTION

For isotropic materials, the thermoelastic constitutive equation can be derived from the thermoelastic matrix (15):

$$\left.\begin{aligned}
\varepsilon_{xx} &= \frac{1}{E}\left[\sigma_{xx} - \mu\left(\sigma_{yy} + \sigma_{zz}\right)\right] + \alpha_e T \\
\varepsilon_{yy} &= \frac{1}{E}\left[\sigma_{yy} - \mu\left(\sigma_{xx} + \sigma_{zz}\right)\right] + \alpha_e T \\
\varepsilon_{zz} &= \frac{1}{E}\left[\sigma_{zz} - \mu\left(\sigma_{xx} + \sigma_{yy}\right)\right] + \alpha_e T \\
\gamma_{xy} &= \frac{\tau_{xy}}{G} \\
\gamma_{yz} &= \frac{\tau_{yz}}{G} \\
\gamma_{xz} &= \frac{\tau_{xz}}{G}
\end{aligned}\right\} \tag{16}$$

where E and G are the elastic modulus and shear modulus of the material, μ is the Poisson's ratio, which is taken as 0.3.

The corresponding stress equation can be obtained from the generalized Hooke's law:

$$\left.\begin{aligned}
\sigma_{xx} &= -E\frac{(1-\mu)\varepsilon_{xx} + \mu\left(\varepsilon_{yy} + \varepsilon_{zz}\right) - \alpha_e T(1+\mu)}{(1+\mu)(-1+2\mu)} \\
\sigma_{yy} &= -E\frac{(1-\mu)\varepsilon_{yy} + \mu\left(\varepsilon_{xx} + \varepsilon_{zz}\right) - \alpha_e T(1+\mu)}{(1+\mu)(-1+2\mu)} \\
\sigma_{zz} &= -E\frac{(1-\mu)\varepsilon_{zz} + \mu\left(\varepsilon_{xx} + \varepsilon_{yy}\right) - \alpha_e T(1+\mu)}{(1+\mu)(-1+2\mu)} \\
\tau_{xy} &= \gamma_{xy} G \\
\tau_{yz} &= \gamma_{yz} G \\
\tau_{xz} &= \gamma_{xz} G
\end{aligned}\right\} \tag{17}$$

The geometry equation for the total strain of the elastomer can be expressed as:

$$\left.\begin{aligned}
\varepsilon_{xx} &= \frac{\partial u}{\partial x}, \gamma_{xy} = \frac{\partial u}{\partial y} + \frac{\partial v}{\partial x} \\
\varepsilon_{yy} &= \frac{\partial v}{\partial y}, \gamma_{yz} = \frac{\partial v}{\partial z} + \frac{\partial w}{\partial y} \\
\varepsilon_{zz} &= \frac{\partial w}{\partial z}, \gamma_{xz} = \frac{\partial u}{\partial z} + \frac{\partial w}{\partial x}
\end{aligned}\right\} \tag{18}$$

where u, v, and w are the displacements in the three directions.

The thermal stress can be calculated from the equilibrium differential equation, which is the Navier equation:

$$\left.\begin{aligned}
\frac{\partial \sigma_{xx}}{\partial x} + \frac{\partial \tau_{xy}}{\partial y} + \frac{\partial \tau_{xz}}{\partial z} + X = 0 \\
\frac{\partial \tau_{xy}}{\partial x} + \frac{\partial \sigma_{yy}}{\partial y} + \frac{\partial \tau_{yz}}{\partial z} + Y = 0 \\
\frac{\partial \tau_{xz}}{\partial x} + \frac{\partial \tau_{yz}}{\partial y} + \frac{\partial \sigma_{zz}}{\partial z} + Z = 0
\end{aligned}\right\} \tag{19}$$

where X, Y, and Z are the components of the force in the three coordinate directions. The stress in the deposition process can be assumed to be caused by forces due to temperature change. Thus, the temperature change is transformed into a solution for thermal loading, known as equivalent thermal loading.

$$\left.\begin{aligned}
X &= -\frac{\alpha_e E}{1-2\mu}\frac{\partial T}{\partial x} \\
Y &= -\frac{\alpha_e E}{1-2\mu}\frac{\partial T}{\partial y} \\
Z &= -\frac{\alpha_e E}{1-2\mu}\frac{\partial T}{\partial z}
\end{aligned}\right\} \tag{20}$$

E. FINITE ELEMENT MODEL

During the LDED process, the material undergoes rapid melting and solidification and multiple heating and cooling cycles. As a result, the deposited parts are subjected to dynamically inhomogeneous temperature variations. During such uneven temperature variations, significant internal stress is generated within the deposited parts, leading to distortion and even cracking of the parts, thereby impacting the quality of the final product [4], [5]. This study was based on the birth-death element technique of ANSYS finite element analysis. The heat source model and the cyclic heat transfer model were created using ANSYS Parametric Design Language (APDL). The APDL command streams were extracted into Workbench to construct the heat transfer model, and it was solved to obtain the temperature field of the model. Subsequently, the calculated results of the temperature field were applied as loads to the stress field using the sequential coupling method. Finally, the analysis of thermal stress and distortion was conducted based on the fundamental equations of thermoelastic-plastic mechanics [10], [25], [26]. To ensure a realistic simulation process, the study employed the "birth-death element" technique to simulate the deposition process of the part. First, the part and the substrate were modeled. Subsequently, all the part elements were killed before loading the heat source. The term "kill" does not refer to the deletion of an element but rather the reduction of material properties by multiplying the stiffness matrix with a minimal factor when the heat source does not reach the element. The level of mesh refinement in the finite element model directly impacts the computational efficiency and accuracy of the simulation analysis solution. Finer mesh division leads to calculation results closer to the actual values but also increases the storage requirements and calculation time. The non-uniform mesh was utilized in this study to achieve a balance between computational efficiency and accuracy. The fine mesh was used in the deposition zone and neighboring zones, while the mesh became progressively coarser as the distance from the deposition zone increased. A total of 17,521 cells and 27,955 nodes were generated. The geometric mesh and scanning path of the finite element model are shown in Fig. 3. The scanning strategy utilized the zigzag path with a 1 mm pitch, and the scanning direction was kept consistent layer by layer. The substrate size was 100 mm × 100 mm × 5 mm, and the deposition layer size was 30 mm × 30 mm × 5 mm. The left side of the substrate served as the clamping end, with a clamping width of 10 mm, allowing for unrestricted distortion at the other end. The simulated process parameters were set as follows: scanning speed was 8 mm/s, laser power was 800 W, spot diameter was 2 mm, scanning pitch was 1 mm, powder feeding speed was 1 rad/min, and layer thickness was 0.5 mm. The emissivity of Inconel 718 was set to 0.7, and the convective heat transfer coefficient was set to 7 W/(m^2·°C). Additionally, the convective heat transfer coefficient was set to 50 W/(m^2·°C) at the clamping end and the bottom of the substrate, considering the heat conduction effect at the contact surface between the fixture and the

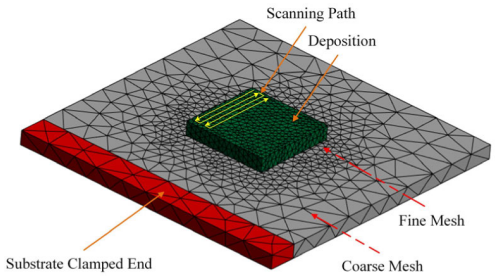

FIGURE 3. Mesh model and scanning path.

substrate. It is important to note that these process parameters were not arbitrarily chosen but correspond to the parameters used in the actual deposit of Inconel 718 alloy parts. The numerical simulations in this study were performed on a workstation equipped with a 16-core processor (4.5GHz) and 64GB of RAM. The total computational time required for the simulations was approximately 16 hours.

F. INITIAL AND BOUNDARY CONDITIONS

The initial temperature condition is:

$$T(x, y, z, t)|_{t=0} = T_0 \tag{21}$$

where T_0 is the surrounding ambient air temperature.

The initial temperature of the metal powder and substrate was assumed to be 25 °C, and it was also assumed that the surrounding ambient air temperature was 25 °C.

The thermal energy exchange in the deposition process is dominated by thermal convection and thermal radiation. Therefore, the thermal boundary condition in the calculation process conforms to the third type of boundary condition:

$$-k\frac{\partial T}{\partial n} = h_c(T - T_0) + \varphi\chi\left(T^4 - T_0^4\right) \tag{22}$$

According to the experimental conditions of the deposition process, the displacement boundary condition was set to impose total displacement constraints on all nodes located at the left clamping end of the substrate.

III. MATERIALS AND METHODS

A. MATERIAL

The material selected for deposition in this study was Inconel 718 spherical powder, prepared by the gas atomization method, with particle sizes ranging from 15 μm to 53 μm. Due to its high stability, creep resistance, strength, and fatigue lifetime is widely used in critical high-temperature components, such as aerospace engine turbines and structural parts in the nuclear power industry [27], [28]. The material used for both the substrate and the deposition layer in the simulations and experiments of this study was Inconel 718 alloy. The chemical composition is presented in Table 1. Before the deposition experiments, the powder was dried under a vacuum at approximately 120 °C to reduce moisture content and improve its fluidity. The surface of the substrate was sanded with sandpaper to remove the oxide film and enhance the laser absorption rate. Subsequently, the substrate surface was cleansed with ethanol to eliminate rust, grease, and dust particles [29].

The LDED deposition process is a rapid solidification and cooling process. The thermodynamic properties of the material undergo nonlinear changes during this process. Suppose the material property parameters are set improperly. In that case, it may result in the termination of numerical simulation due to the non-convergence of the differential equation solution or significant discrepancies between the calculated and actual results. By reviewing relevant literature, the thermomechanical property parameters of Inconel 718 alloy are presented in Fig. 4 [30], [31], [32], [33], [34].

B. EXPERIMENTAL SETUP

To validate the cyclic thermodynamic coupling model proposed in this study, parts were deposited using the Raycham LDM 4030 metal deposition system. The system is equipped with a fiber laser that operates at a wavelength of 1080 nm and has a maximum output power of 1500 W. The deposition process was conducted in a sealed chamber with an argon atmosphere. The experimental process parameters were consistent with the simulation parameters.

The temperature and distortion measurement system utilized in this study is illustrated in Fig. 5. Experimental measurements were conducted to validate the temperature and distortion predicted by the model. The in-situ temperature was measured using a 1 mm diameter K-type thermocouple with an uncertainty of ±0.75%. The thermocouple signal was recorded using the data acquisition instrument (TA612C). The in-situ temperature measurement positions (T1 and T2) were chosen to be as close to the heat source as possible while maintaining a sufficient distance to avoid thermocouple damage, as shown in Fig. 6. It is essential to note that ideally, the probe tip of the thermocouple is not a point but has a specific area. As a result, the temperature measured by the thermocouple represents the average value within that contact area. In this study, the SICK OD2 high-precision laser displacement sensor was utilized to measure the distortion of the substrate in the build direction (Z-direction). The sensor has a range of 26 mm, and the measurement uncertainty is ±0.02%. The Smart lab type X-ray diffractometer

TABLE 1. Chemical composition of Inconel 718 alloy powder (weight percent).

Elements	Ni	Cr	Nb	Mo	Mn	Si	Al	Cu	Ti	C	Fe
wt.%	51.71	18.93	5.12	3.08	0.13	0.14	0.49	0.05	0.97	0.04	Bal.

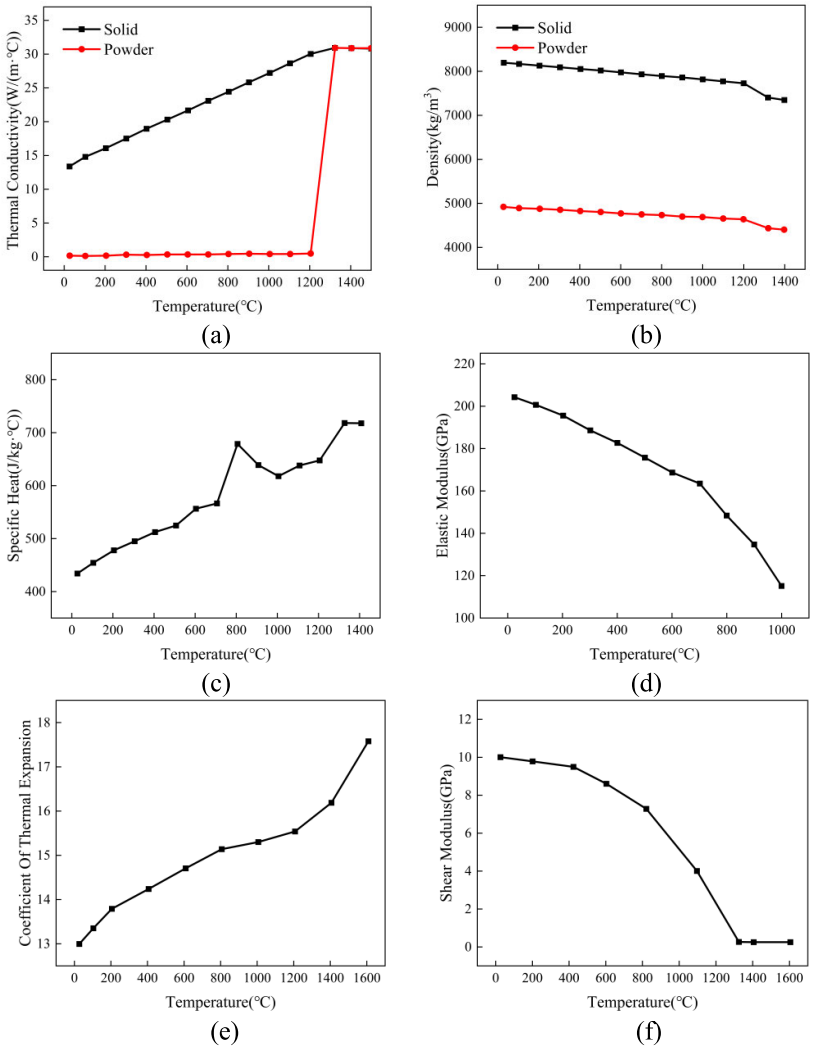

FIGURE 4. Thermomechanical property parameters of Inconel 718: (a) Thermal conductivity; (b) Density; (c) Specific heat; (d) Elastic modulus; (e) Coefficient of thermal expansion; (f) Shear modulus [30], [31], [32], [33], [34].

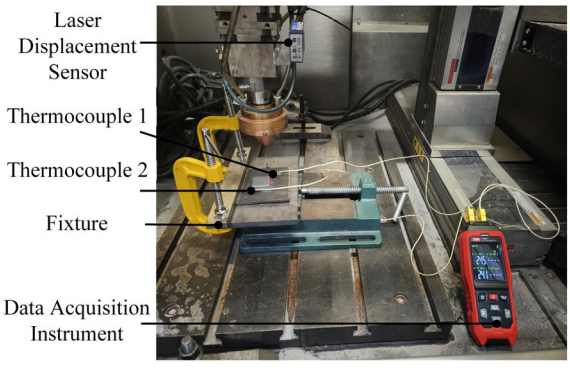

FIGURE 5. Temperature and distortion measurement system.

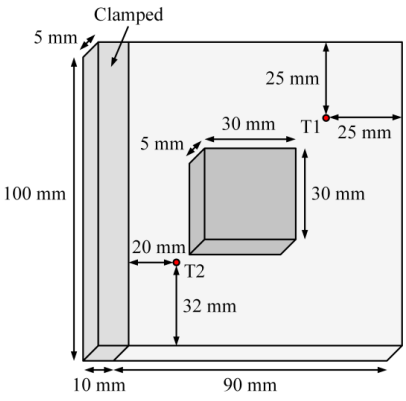

FIGURE 6. Locations of temperature measurement points.

from Rigaku, Japan, was used to measure the residual stress on the part's surface. The experimental results were then compared to the predicted residual stress from the model. The locations of the measurement points (S1-S3) are shown in Fig. 7. S1 and S2 were positioned on the upper surface of the substrate, while S3 was located on the top surface of

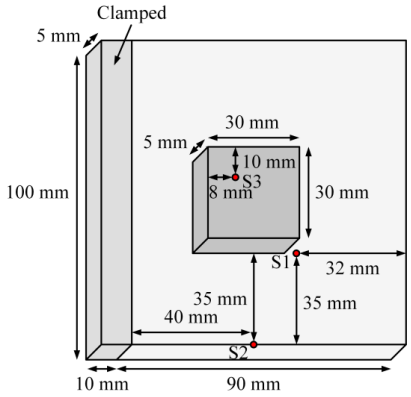

FIGURE 7. Locations of residual stress measurement points.

the part. Three measurements were taken at each point, and then the measurements were averaged. It is important to note that the samples were not cleaned, ground, or polished before testing to prevent the introduction of artificial stress.

IV. RESULTS AND DISCUSSION

A. TEMPERATURE FIELD EVOLUTION

1) COMPARISON OF MEASURED AND SIMULATED TEMPERATURE

The thermal response curves of the T1 and T2 points during the deposition process are calculated using the cyclic heat transfer model established in the previous section. These curves are compared to the actual measurement results obtained from the thermocouples, as shown in Fig. 8. The average errors between the simulation and experimental results for the T1 and T2 points are 2.05% and 4.48%, respectively. The thermal cycling process between the simulated and measured curves is generally consistent, and the thermal response curves of each test point exhibit similar evolutionary characteristics. This finding demonstrates the accurate prediction of temperature evolution during the deposition process by the cyclic heat transfer model. The potential factors contributing to the errors include measurement errors caused by differences in thermocouple potential and deviations in material parameters defined by the numerical model from the actual material properties. During the deposition process, the temperature profile exhibits a regular fluctuating increase. This increase is primarily attributed to the laser heat source's periodic movement and heat accumulation layer-by-layer. As the deposition process continues, the heat input from the laser heat source significantly exceeds the heat loss. Consequently, heat accumulates gradually on the substrate, leading to a rise in substrate temperature. After the deposition process concludes, there is no further heat input, resulting in a gradual dissipation of the accumulated thermal energy and subsequent substrate cooling. It is important to note that the temperature at point T2 reaches a peak of approximately 160 °C higher than at point T1. This discrepancy can be attributed to the closer proximity of point T2 to the heat-affected zone, causing more significant heat accumulation in that particular region.

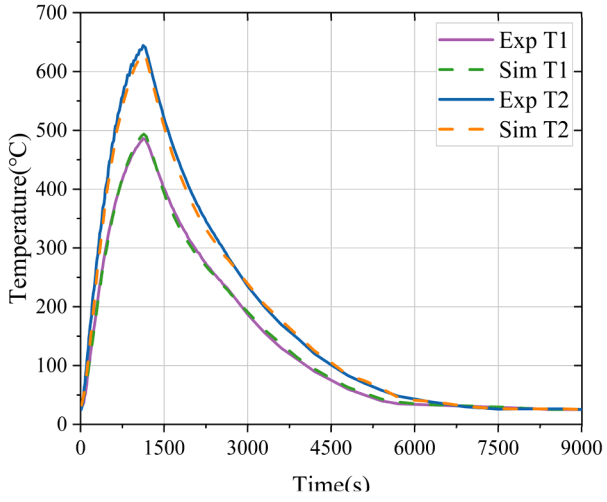

FIGURE 8. Comparison of measured and simulated temperature.

2) TEMPERATURE DISTRIBUTION

Fig. 9 illustrates the temperature distribution at six different time points. As the additive process progresses, the heat accumulation effect becomes evident. The temperature of the molten pool steadily increases from 1570.59 °C in Fig. 9(a) to 1803.11 °C in Fig. 9(f). Comparing the temperature field distribution of the substrate across the six graphs, it can be observed that the minimum temperature rises from room temperature to 258.073 °C with an increase in the deposition height. By comparing the temperature distribution of the substrate depicted in the six graphs, it becomes apparent that an increase in deposition height leads to the initial expansion of the high-temperature region of the substrate (Fig. 9(a) to Fig. 9(b)). This expansion is followed by a period of relative stability (Fig. 9(b) to Fig. 9(d)) and eventually a contraction, with the high-temperature area trending closer to the part's projected area (Fig. 9(d) to Fig. 9(f)). With an increasing number of deposition layers, the distance between the heat source and the substrate also increases. As a result, the transfer of energy from the laser to the substrate decreases, reducing the size of the heat-affected zone. As further observed in Fig. 9, the heat-affected zone during layer-by-layer deposition is clearly visible. It extends horizontally, resulting in partial remelting of the adjacent melt tracks. Furthermore, the heat-affected zone has 4-5 layers along the downward cross-sectional direction, which heat and remelt the previously deposited layers. This indicates that the temperature field is involved in the cumulative calculation in the cyclic heat transfer model. It also suggests that the aforementioned cyclic heat transfer model aligns with the actual temperature distribution.

Fig. 10 depicts the temperature distribution during the cooling process. The same legend is used for all four figures to observe the cooling process in the high-temperature

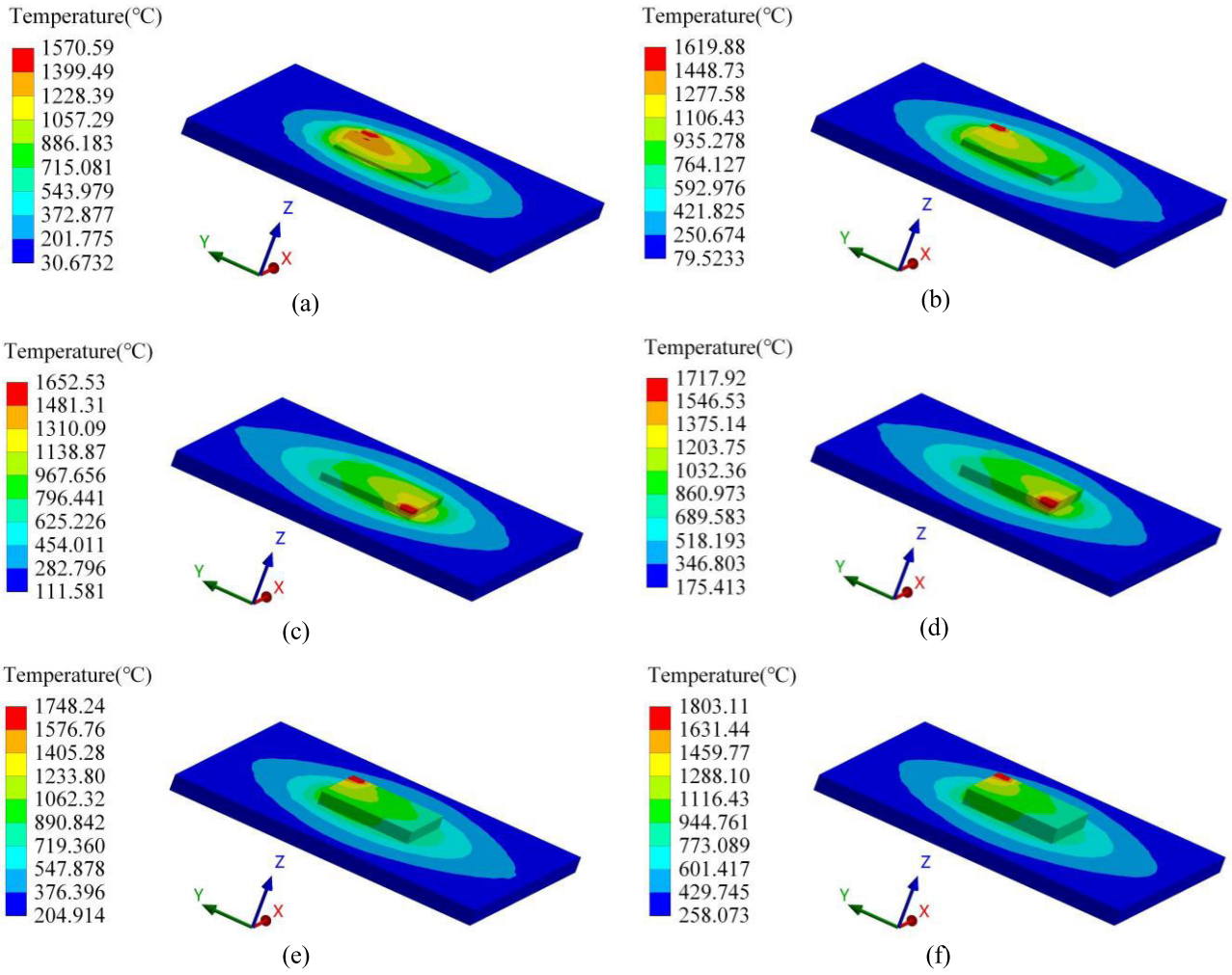

FIGURE 9. Model predicts temperature distribution during the deposition process: (a) 224.5 s (2nd layer); (b) 449 s (4th layer); (c) 561.25 s (5th layer); (d) 785.75 s (7th layer); (e) 898 s (8th layer); (f) 1122.5 s (10th layer).

region. It can be observed that the temperature of the part varies significantly with increasing cooling time. The peak temperature continues to decrease rapidly from 651.362 °C (Fig. 10(a)), 586.713 °C (Fig. 10(b)), 529.359 °C (Fig. 10(c)), to 513.284 °C (Fig. 10(d)). The isothermal surface moves from the substrate towards the top of the part, and a significant amount of heat is dissipated through the part surface into the surrounding environment. However, during the cooling process, except for the high-temperature region located at the bottom of the part, which keeps shrinking, the temperature change in the rest of the region is insignificant. Moreover, the minimum temperature of the substrate decreased slowly from 39.6372 °C (Fig. 10(a)), 39.5804 °C (Fig. 10(b)), 39.4915 °C (Fig. 10(c)), to 39.4593 °C (Fig. 10(d)). It can be observed that during the cooling process, the substrate and the deposited part cool down extremely unevenly, with the part experiencing a significantly more drastic decrease in temperature.

B. STRESS FIELD EVOLUTION

1) COMPARISON OF MEASURED AND SIMULATED SURFACE RESIDUAL STRESS

Fig. 11 compares the surface residual stress measured by X-ray diffraction with the simulated results. The errors between the simulated and measured results at S1, S2, and S3 are 10.19%, 12.31%, and 11.86%, respectively. Although there are some discrepancies between the simulated and measured results, they exhibit overall consistency. This finding offers supporting evidence for the reliability of the cyclic thermodynamic coupling model established in this study in predicting residual stress. The errors observed in this study can be attributed to several factors. First, the numerical simulation ignores the solid-liquid phase transition, affecting residual stress's generation and evolution. Secondly, residual stress measurement using X-ray diffraction is susceptible to reflection errors from the crystal surface, resulting in specific errors in the experimental measurements. As shown

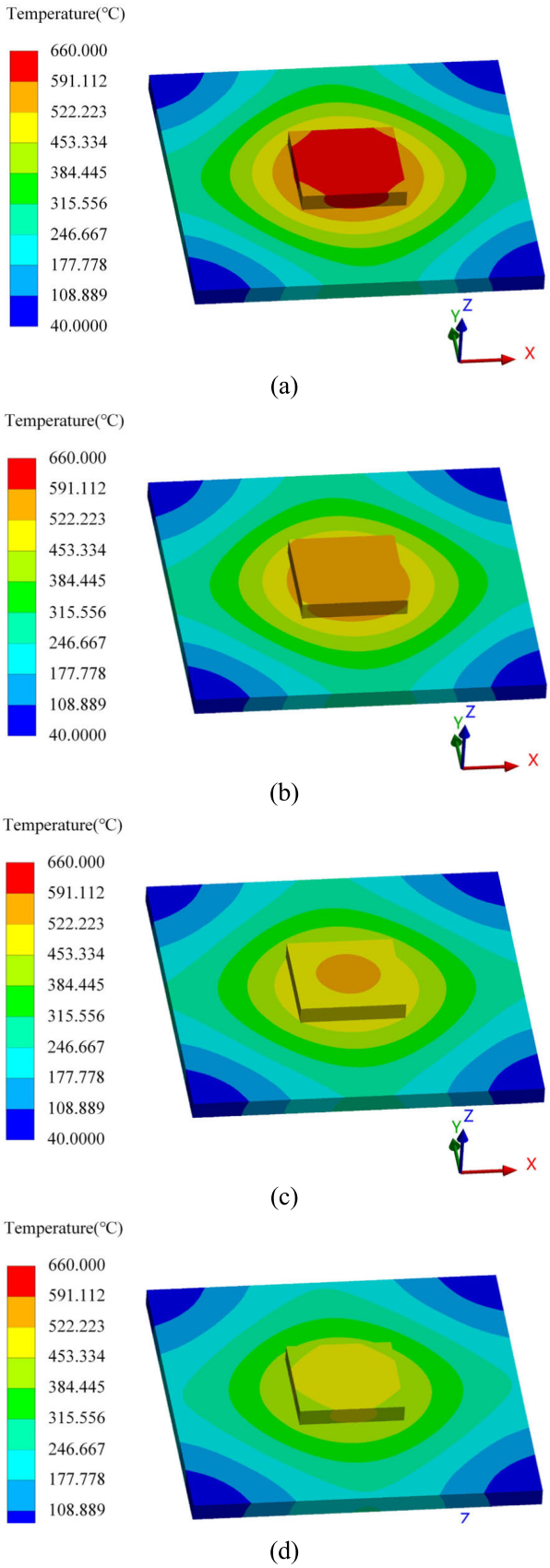

FIGURE 10. Model predicts temperature distribution during the cooling process: (a) Cooling 600 s; (b) Cooling 700 s; (c) Cooling 900 s; (d) Cooling 1000 s.

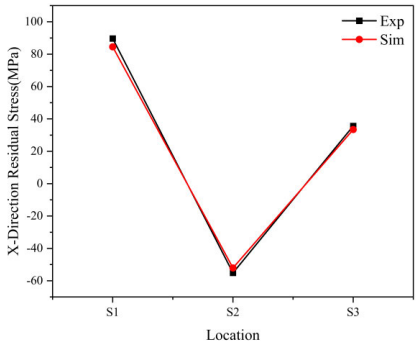

FIGURE 11. Comparison of measured and simulated X-direction residual stress.

in Fig. 11, the S1 point is situated in the heat-affected zone, exhibiting tensile stress in the X-direction. The S2 point is located at the edge of the substrate, where the part experiences shrinkage in the X-direction, resulting in compressive stress. The S3 point is positioned on the top surface of the part, where the tensile stress on the surface is minimal, and the X-direction residual stress is a relatively small positive value.

2) STRESS DISTRIBUTION

Fig. 12 illustrates the variation in stress distribution at different time points. The stress distribution undergoes significant changes over time. Towards the end of the deposition of the 1st layer (Fig. 12(a)), a majority of the substrate still remains in a cold state. Consequently, a large temperature gradient exists, resulting in the highest stress value at this moment, reaching 380.118 MPa. As the number of deposition layers increases, the high-temperature region expands, the temperature gradient decreases, and the stress decreases. By the end of the 4th layer (Fig. 12(b)), the maximum stress decreases to its lowest value of 102.019 MPa during the deposition process. However, the stress at the clamping end of the left side of the substrate has stabilized. As the additive manufacturing progresses, the stress value slowly recovers, and by the end of the 7th layer (Fig. 12(c)), the stress value increases to 137.652 MPa. By the end of the deposition process (Fig. 12(d)), the maximum stress reaches 169.229 MPa. The high-stress areas are concentrated in the substrate beneath the part and in its vicinity. The peak stress is found at the four corners where the part comes into contact with the substrate. This indicates that the stress gradually accumulates in the bottom layer as the thermal action cycles, and the stress decreases significantly as the location gets closer to the part's surface. This implies that the stress is higher in the bottom layer near the substrate due to the effect of cyclic accumulation. Simultaneously, the clamping end of the substrate gradually concentrates a portion of the stress, influenced by lower temperature and constraint in all three directions of freedom.

Fig. 13 illustrates the residual stress distribution at cooling 3000 s (Fig. 13(a) and Fig. 13(c)) and cooling to room temperature (Fig. 13(b) and Fig. 13(d)). Fig. 13(a) and Fig. 13(b)

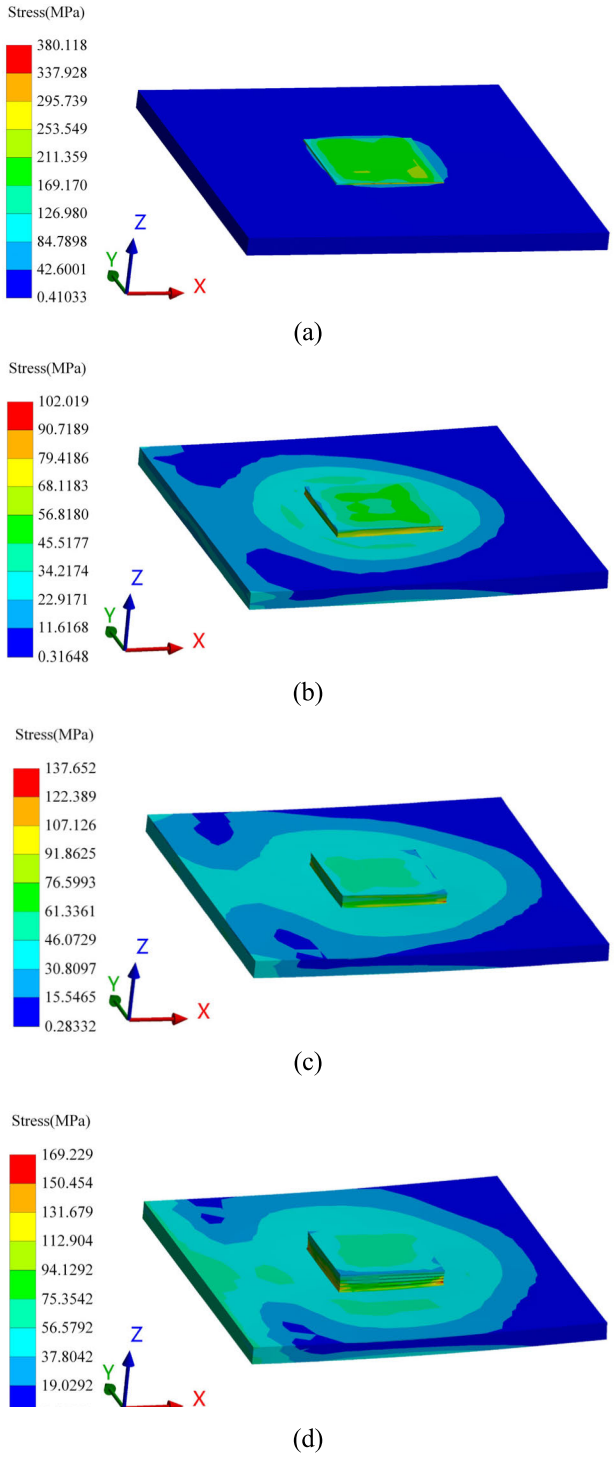

FIGURE 12. Model predicts stress distribution during the deposition process: (a) 112.25 s (1st layer); (b) 449 s (4th layer); (c) 785.75 s (7th layer); (d) 1122.5 s (10th layer).

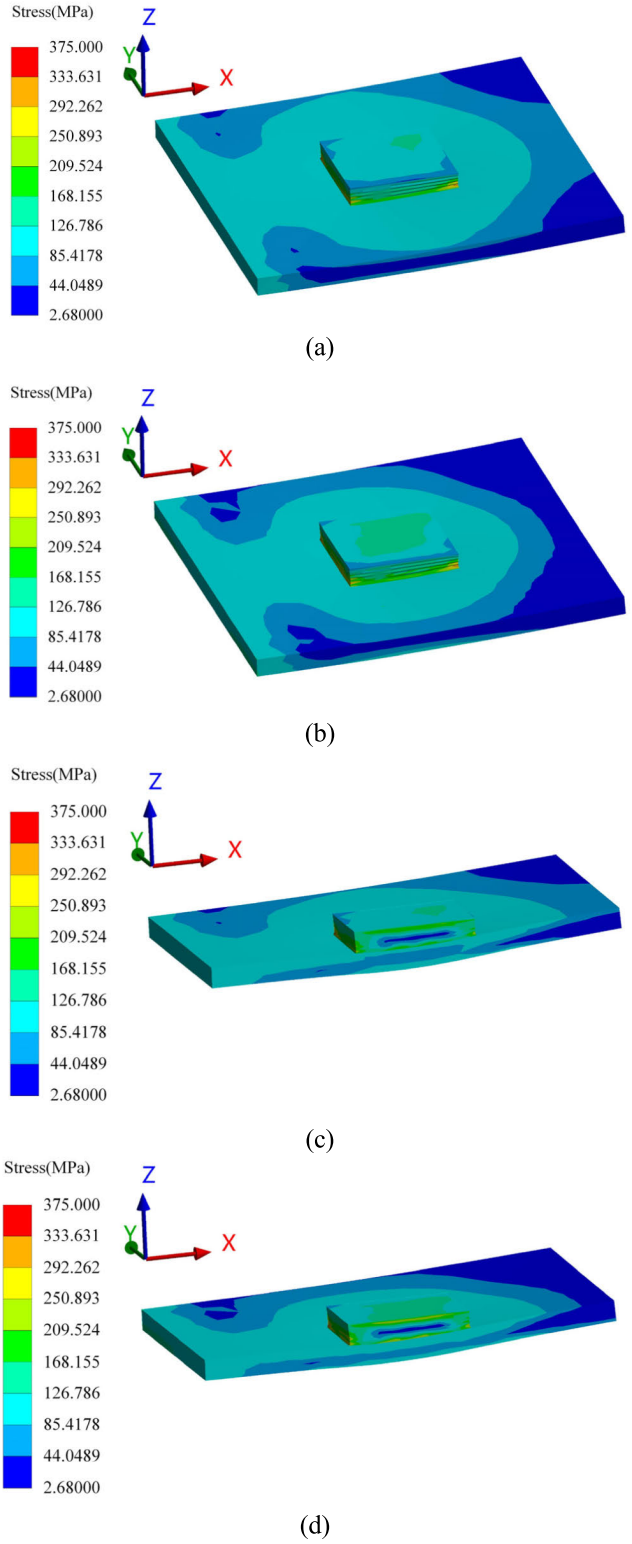

FIGURE 13. Model predicts residual stress distribution during the cooling process: (a) Cooling 3000 s; (b) Cooling to room temperature; (c) Half-section view of cooling 3000 s; (d) Half-section view of cooling to room temperature.

show the complete view, while Fig. 13(c) and Fig. 13(d) show the half-section view, in which the front half is retained following sectioning along the anterior-posterior (Y-direction) symmetry plane to enable observation of stress distribution inside. By comparing Fig. 13(a) and Fig. 13(b), it can be observed that the peak residual stress increases from 347.648 MPa to 372.583 MPa as the cooling time increases. The stress at the clamping end of the substrate remains

relatively stable, exhibiting less variation in distribution characteristics and values. Due to the rigid constraint of the substrate on the combined area of the part and substrate during the cooling process, the relative distortion between them is hindered and constrained. As a result, the combined area exhibits the highest residual stress, which is considered a critical zone prone to distortion and cracking. A similar analysis can be found in [35] and [36]. Optimizing the process parameters during the actual deposition process helps maintain low residual stress in the part, leading to better performance and increased safety. Although the peak residual stress value in the part is lower than the yield strength of Inconel 718 when cooled to room temperature, they still hold value for study. As indicated in Fig. 13(a) and Fig. 13(b), the peak stress consistently occurs at the four corners where the part and substrate come into contact. Furthermore, the stress level escalates with prolonged cooling time. To acquire the stress distribution inside the component,

Fig. 13(a) and Fig. 13(b) are semi-dissected to obtain Fig. 13(c) and Fig. 13(d). Through comparison, it is evident that the stress distribution characteristics vary between the surface and interior of the part. The high-stress region on the surface appears to be more extensive, possibly due to the significant convective heat transfer effect and more pronounced temperature variations compared to the interior. In Fig. 13(c) and Fig. 13(d), it can be observed that the partition interface between the part and the substrate traverses through the striped region of high-stress concentration, where stress value progressively increases with longer cooling time.

Fig. 14 illustrates the stress curves at three points, A, B, and C, during the deposition process. Points A and B are located on the upper surface of the substrate, while point C is positioned at the center of the deposited part. As shown in Fig. 14, the general trend of the stress curves at points A and B is the same. Initially, there is a significant fluctuating decrease, followed by a gradual increase and a rapid upward movement during the final cooling phase. Points A and B are located on the upper surface of the substrate. Significant transient stress changes can be observed during the initial deposition stage at these points. However, as the number of deposited layers increases, the stress amplitude gradually decreases, leading to a gradual weakening effect on the test points. As the height of deposition increases, the distance between the heat source and the test points also increases. Therefore, the influence and constraints on the test points gradually reduce. Point C is located inside the part at a higher temperature, maintaining a relatively low-stress value. In the later stage, the stress value of all three curves gradually increases, and the slope of the stress curves becomes steeper during the cooling stage. This indicates that the cooling stage has a more significant impact on the stress level.

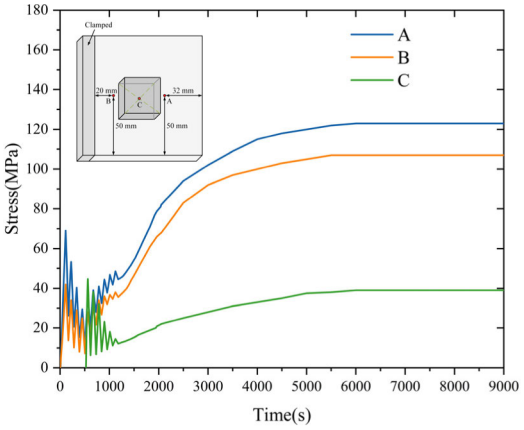

FIGURE 14. Model predicts stress time curves of three test points.

C. DISTORTION EVOLUTION

1) COMPARISON OF MEASURED AND PREDICTED SUBSTRATE DISTORTION

During the deposition process, the left side of the substrate was fixed, while the right side had unrestricted degrees of freedom, resulting in longitudinal warpage distortion as the primary form of distortion. After the deposition was completed and the part was cooled to room temperature, the distortion of the substrate in the build direction (Z-direction) was measured using a laser displacement sensor. Fig. 15 illustrates the predicted and measured substrate distortion results. The predicted maximum substrate distortion is 4.361 mm, whereas the actual maximum distortion is 4.206 mm, resulting in an error of 3.69%. The location of the maximum distortion point is at the corner (marked by a red circle), which is away from the clamped end. These values exhibit a

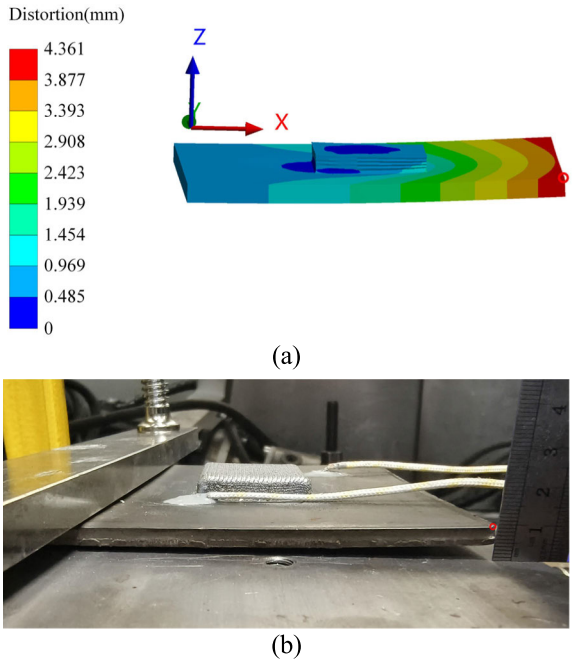

FIGURE 15. Comparison of predicted and measured substrate distortion: (a) Predicted substrate distortion results; (b) Measured substrate distortion results.

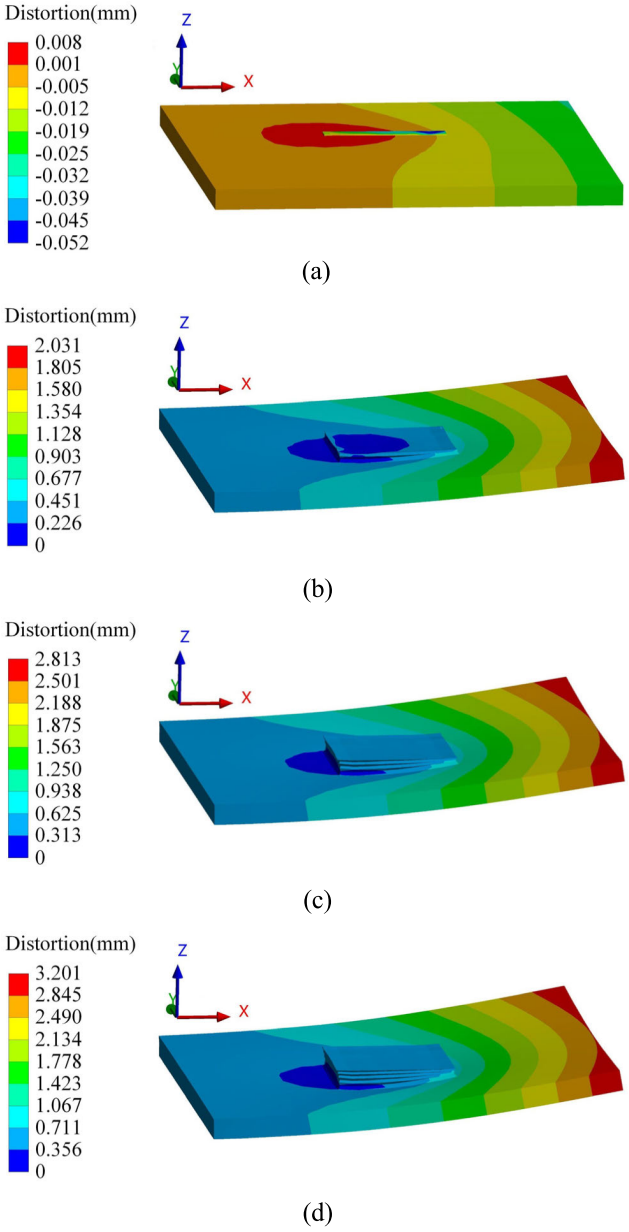

FIGURE 16. Model predicts distortion history during the deposition process: (a) 3.75 s (1st track); (b) 449 s (4th layer); (c) 785.75 s (7th layer); (d) 1122.5 s (10th layer).

relatively consistent trend, providing strong evidence for the reliability of the predicted distortion based on the cyclic thermodynamic coupling model established in this study. Despite the similarity between the predicted substrate distortion and the measured results, some errors still persist. One potential contributing factor is the initial deposition process, wherein the substrate temperature is lower, leading it to absorb heat from the molten pool. This results in a thinner deposition layer thickness. As the number of deposition layers increases, the substrate temperature rises, and the deposition layer thickness stabilizes. However, the numerical model assumes that the thickness of all deposition layers is the average layer thickness, introducing errors into the model.

2) DISTORTION HISTORY

The magnitude and direction of substrate distortion continuously change over time during the deposition process. Fig. 16 depicts the schematic diagram of Z-direction distortion at four time nodes (magnified three times). At 3.75 s (Fig. 16(a)), the 1st track of the 1st layer finishes scanning. With the short deposition time, the molten pool's transient thermal expansion exceeds the deposited tracks' continuous cooling contraction and heat-affected zone, causing the substrate distortion to bend downward. At 449 s (Fig. 16(b)), four layers have been formed. As the heat-affected zone continues to cool and contract, it induces a change in the substrate distortion direction, leading to upward warpage distortion. This indicates the transient nature of the distortion, highlighting its dynamic behavior. This phenomenon is because when the heat source departs, the deposition area rapidly cools and contracts. However, at this moment, the substrate is in a state of rapid heat absorption and warming, causing a decrease in its yield limit after the temperature rises. When the substrate thermal expansion is constrained by the rigidity of the surrounding cold metal, it can only be released towards the weakest portion of the substrate below. Consequently, this effect also results in upward warping distortion at the free end of the substrate. At 785.75 s (Fig. 16(c)) and 1122.5 s (Fig. 16(d)), the substrate continues to exhibit upward warping, although the numerical rate of warping decreases. Fig. 17 demonstrates the Z-direction distortion diagrams (magnified three times) at cooling 700 s and cooling 800 s, respectively.

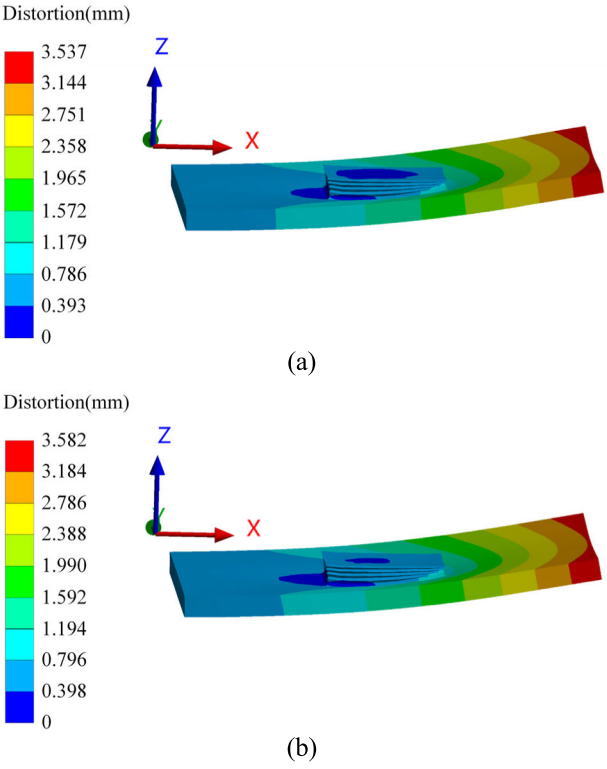

FIGURE 17. Model predicts distortion history during the cooling process: (a) Cooling 700 s; (b) Cooling 800 s.

TABLE 2. Comparison of the prediction accuracy of the proposed model in this study with the existing finite element models.

Model	Material	Prediction Accuracy		
		Temperature	Residual Stress	Distortion
Yang et al. [8]	Inconel 718	\	\	96.85%
Nain et al. [11]	316L	96.95%	\	\
Dantin et al. [16]	Ti-6Al-4V	94.95%	\	\
Fang et al. [34]	Inconel 718	84.71%	\	\
Zeng et al. [36]	#45 steel	\	86.70%	\
Li et al. [37]	AISI 4140	\	84.85%	\
Pourabdollah et al. [9]	Ti-6Al-4V	89.04%	\	85.79%
Kiran et al. [10]	316L	86.13%	81.26%	\
Kiran et al. [17]	316 L	80.91%	75.64%	\
Yan et al. [24]	316L	96.62%	82.35%	\
Weisz-Patrault et al. [38]	316L	81.32%	\	86.88%
Nain et al. [39]	316L	89.57%	\	95.65%
Cooke et al. [7]	42CrMo4	94.44%	44.74%	83.77%
This study	Inconel 718	96.74%	88.55%	96.31%

As evident from the figure, as the cooling time prolongs, both the part and the substrate undergo continuous cooling and contraction, leading to a gradual increase in the warpage distortion of the substrate. Approximately 26% of the distortion is attributed to the cooling stage, meaning that the more significant temperature gradient contributes to the warpage distortion of the part.

The prediction accuracy of the model proposed in this study was compared with previous work, as shown in Table 2. It can be seen that the model proposed in this study is at the stage of being equal to or slightly ahead in prediction accuracy for a single indicator alone. However, there is a clear advantage in the number of prediction indexes, allowing for simultaneous high-precision temperature, residual stress, and distortion predictions. This capability is not available in existing finite element models.

V. CONCLUSION AND FUTURE DIRECTION

In this study, we develop a cyclic thermodynamic coupling model based on the cyclic temperature field and the cumulative stress field during the LDED process. This model aims to predict temperature, residual stress, and distortion evolution. The prediction results are substantiated through actual deposition experiments, showcasing high prediction accuracy. Furthermore, the analysis also encompasses the assessment of temperature, residual stress, and distortion history. Based on the results of the study and the subsequent discussion, the following conclusions can be drawn:

1) The established cyclic thermodynamic coupling model can effectively calculate the layer-by-layer superposition of thermal effects during the deposition process and the cyclic accumulation of thermal stress, which improves the model's prediction accuracy. The prediction accuracy of temperature, residual stress, and distortion can reach 96.74%, 88.55%, and 96.31%, respectively.

2) During the deposition process, the temperature of the molten pool continues to rise. The heat-affected zone extends both horizontally and cross-sectionally. During the cooling process, the substrate and the deposited part cool down extremely unevenly, with the part experiencing a significantly more drastic decrease in temperature. The isothermal surface moves from the substrate towards the top of the part, and a significant amount of heat is dissipated through the part surface into the surrounding environment.

3) During the deposition process, the stress gradually accumulates in the bottom layer as the thermal action cycles. The high-stress areas are concentrated in the substrate beneath the part and in its vicinity. The peak stress is found at the four corners where the part comes into contact with the substrate. During the cooling process, the bonding area between the part and substrate is constrained by the rigidity of the substrate. Consequently, the bonding area experiences the highest level of residual stress, which increases as the cooling time extends.

4) The magnitude and direction of substrate distortion vary continuously during the deposition process. The point of maximum distortion is located at the corner point away from the clamping end. The part and substrate undergo continuous cooling and shrinkage during the cooling process. As a result, the substrate experiences warpage distortion that

progressively increases, resulting in a distortion of approximately 26%.

In this study, significant research results have been achieved in predicting the temperature, residual stress, and distortion evolution during the LDED process. These findings provide a solid foundation for the next phase of the study. The upcoming phase will concentrate on methods to release and correct the generated residual stress and distortion to enhance the deposition quality of parts.

REFERENCES

[1] M. Murua, A. suárez, D. Galar, and R. Santana, "Tool-path problem in direct energy deposition metal-additive manufacturing: Sequence strategy generation," *IEEE Access*, vol. 8, pp. 91574–91585, 2020.

[2] W. Guoqing, H. Yingzhou, Z. Weinan, S. Chenguang, and H. Hongsong, "Research status and development trend of laser additive manufacturing technology," in *Proc. 4th Int. Conf. Inf. Sci. Control Eng. (ICISCE)*, Changsha, China, Jul. 2017, pp. 1210–1213.

[3] F. Wang, S. Fathizadan, F. Ju, K. Rowe, and N. Hofmann, "Print surface thermal modeling and layer time control for large-scale additive manufacturing," *IEEE Trans. Autom. Sci. Eng.*, vol. 18, no. 1, pp. 244–254, Jan. 2021.

[4] E. Mirkoohi, J. R. Dobbs, and S. Y. Liang, "Analytical modeling of residual stress in direct metal deposition considering scan strategy," *Int. J. Adv. Manuf. Technol.*, vol. 106, nos. 9–10, pp. 4105–4121, Feb. 2020.

[5] E. Mirkoohi, J. R. Dobbs, and S. Y. Liang, "Analytical mechanics modeling of in-process thermal stress distribution in metal additive manufacturing," *J. Manuf. Processes*, vol. 58, pp. 41–54, Oct. 2020.

[6] D. Yushu, M. D. Mcmurtrey, W. Jiang, and F. Kong, "Directed energy deposition process modeling: A geometry-free thermo-mechanical model with adaptive subdomain construction," *Int. J. Adv. Manuf. Technol.*, vol. 122, no. 2, pp. 849–868, Sep. 2022.

[7] S. Cooke, G. Sweet, K. Ahmadi, P. Bishop, and R. Herring, "Thermo-mechanical-metallurgical modelling, validation and characterization of 42CrMo4 steel processed by directed energy deposition," *J. Manuf. Processes*, vol. 81, pp. 537–561, Sep. 2022.

[8] G. Yang, B. Liu, L. Li, P. Li, X. Meng, Z. Xu, and J. Zhou, "In situ measurement and numerical simulation on deformation in laser depositing inconel 718," *J. Brazilian Soc. Mech. Sci. Eng.*, vol. 44, no. 11, Nov. 2022, Art. no. 503.

[9] P. Pourabdollah, F. Farhang Mehr, D. M. Maijer, and S. L. Cockcroft, "A novel approach for the numerical analysis of in situ distortion in a component made by the directed energy deposition additive manufacturing process," *Int. J. Adv. Manuf. Technol.*, vol. 124, nos. 5–6, pp. 1925–1938, Jan. 2023.

[10] A. Kiran, J. Hodek, J. Vavřík, M. Urbánek, and J. Džugan, "Numerical simulation development and computational optimization for directed energy deposition additive manufacturing process," *Materials*, vol. 13, no. 11, p. 2666, Jun. 2020.

[11] V. Nain, T. Engel, M. Carin, D. Boisselier, and L. Seguy, "Development of an elongated ellipsoid heat source model to reduce computation time for directed energy deposition process," *Frontiers Mater.*, vol. 8, Dec. 2021, Art. no. 747389.

[12] F. Vignat, N. Béraud, and F. Villeneuve, "Rapid thermal simulation of powder bed additive manufacturing," in *Proc. IEEE Int. Conf. Ind. Eng. Eng. Manage. (IEEM)*, Bangkok, Thailand, Dec. 2018, pp. 1498–1502.

[13] D. Mukin, E. Valdaytseva, G. Turichin, and A. Vildanov, "An extended analytical solution of the non-stationary heat conduction problem in multi-track thick-walled products during the additive manufacturing process," *Materials*, vol. 14, no. 23, p. 7291, Nov. 2021.

[14] M. Ansari, M. Khamooshi, Y. Huang, and E. Toyserkani, "Analytical solutions for rapid prediction of transient temperature field in powder-fed laser directed energy deposition based on different heat source models," *Appl. Phys. A, Solids Surf.*, vol. 127, no. 6, Jun. 2021, Art. no. 445.

[15] A. Paul, M. Mozaffar, Z. Yang, W. K. Liao, A. Choudhary, J. Cao, and A. Agrawal, "A real-time iterative machine learning approach for temperature profile prediction in additive manufacturing processes," in *Proc. IEEE Int. Conf. Data Sci. Adv. Analytics (DSAA)*, Washington, DC, USA, Oct. 2019, pp. 541–550.

[16] M. J. Dantin, W. M. Furr, and M. W. Priddy, "Toward a physical basis for a predictive finite element thermal model of the LENS™ process leveraging dual-wavelength pyrometer datasets," *Integrating Mater. Manuf. Innov.*, vol. 11, no. 3, pp. 407–417, Sep. 2022.

[17] A. Kiran, Y. Li, J. Hodek, M. Brázda, M. Urbánek, and J. Džugan, "Heat source modeling and residual stress analysis for metal directed energy deposition additive manufacturing," *Materials*, vol. 15, no. 7, p. 2545, Mar. 2022.

[18] Y. Liu, Q. Li, Z. Ren, Z. Jiang, H. Luo, and X. Zhang, "Effect of process parameters on stress field of laser additive manufacturing," *Machines*, vol. 10, no. 12, p. 1197, Dec. 2022.

[19] S. Sahoo, "Prediction of residual stress and deformation of build part with variation of hatch spacing in direct metal laser sintering of AlSi10Mg built part: Thermo-mechanical modeling," *J. Laser Appl.*, vol. 33, no. 3, Aug. 2021, Art. no. 032011.

[20] A. M. Jonaet, H. S. Park, and L. C. Myung, "Prediction of residual stress and deformation based on the temperature distribution in 3D-printed parts," *Int. J. Adv. Manuf. Technol.*, vol. 113, nos. 7–8, pp. 2227–2242, Apr. 2021.

[21] E. G. Park, J. W. Kang, J. Y. Cho, and J. H. Kim, "Calibration technique of thermal analysis model for metal additive manufacturing process simulation by nonlinear regression and optimization," *Appl. Sci.*, vol. 11, no. 24, p. 11647, Dec. 2021.

[22] N. A. Apetre, J. G. Michopoulos, J. C. Steuben, A. J. Birnbaum, and A. P. Iliopoulos, "Analytical thermoelastic solutions for additive manufacturing processes," *Additive Manuf.*, vol. 56, Aug. 2022, Art. no. 102892.

[23] C. Wang, D. T. Pham, C. Wu, J.-W. Kim, S. Su, and Z. Jin, "Artificial thermal strain method: A novel approach for the analysis and fast prediction of the thermal distortion," *J. Mater. Process. Technol.*, vol. 289, Mar. 2021, Art. no. 116937.

[24] Z. Yan, X. Zou, S. Li, G. Luo, and L. Song, "A study on the thermo-mechanical history, residual stress, and dynamic recrystallization mechanisms in additively manufactured austenitic stainless steels," *Metals*, vol. 12, no. 7, p. 1109, Jun. 2022.

[25] F. M. Abdullah, S. Anwar, and A. Al-Ahmari, "Thermomechanical simulations of residual stresses and distortion in electron beam melting with experimental validation for Ti-6Al-4V," *Metals*, vol. 10, no. 9, p. 1151, Aug. 2020.

[26] F.-Z. Sun, Y. Li, Y.-X. Fu, W.-D. Tan, S.-Q. Feng, and M. Pang, "Study on the influence of laser power variation on the temperature field of laser additive manufacturing airport fuel supply pipe network," *Optik*, vol. 221, Nov. 2020, Art. no. 165301.

[27] L. Shu, Z. Heng, P. Li, H. Wu, J. Li, and J. Feng, "Effect of laser powers on the mechanical properties 27SiMn steel with inconel 718 cladding coatings," *Mater. Res. Exp.*, vol. 9, no. 9, Sep. 2022, Art. no. 096511.

[28] P. Promoppatum and V. Uthaisangsuk, "Part scale estimation of residual stress development in laser powder bed fusion additive manufacturing of inconel 718," *Finite Elements Anal. Design*, vol. 189, Jul. 2021, Art. no. 103528.

[29] V. P. Kumar and A. V. Jebaraj, "Microscale investigations on additively manufactured inconel 718: Influence of volumetric energy density on microstructure, texture evolution, defects control and residual stress," *Appl. Phys. A*, vol. 129, no. 5, May 2023, Art. no. 370.

[30] F. Caiazzo, V. Alfieri, G. Corrado, and P. Argenio, "Mechanical properties of inconel 718 in additive manufacturing via selective laser melting: An investigation on possible anisotropy of tensile strength," in *Proc. IEEE 3rd Int. Forum Res. Technol. Soc. Ind. (RTSI)*, Modena, Italy, Sep. 2017, pp. 1–4.

[31] C. Lu and J. Shi, "Simultaneous consideration of relative density, energy consumption, and build time for selective laser melting of inconel 718: A multi-objective optimization study on process parameter selection," *J. Cleaner Prod.*, vol. 369, Oct. 2022, Art. no. 133284.

[32] J.-R. Hwang, J.-Y. Zheng, P.-C. Kuo, C.-D. Huang, and C.-P. Fung, "Process optimization of inconel 718 alloy produced by laser powder bed fusion," *Metals*, vol. 12, no. 9, p. 1494, Sep. 2022.

[33] N. Kladovasilakis, P. Charalampous, K. Tsongas, I. Kostavelis, D. Tzovaras, and D. Tzetzis, "Influence of selective laser melting additive manufacturing parameters in inconel 718 superalloy," *Materials*, vol. 15, no. 4, p. 1362, Feb. 2022.

[34] L. Fang, L. Cheng, J. A. Glerum, J. Bennett, J. Cao, and G. J. Wagner, "Data-driven analysis of process, structure, and properties of additively manufactured inconel 718 thin walls," *NPJ Comput. Mater.*, vol. 8, no. 1, Jun. 2022, Art. no. 126.

[35] T. Machirori, F. Q. Liu, Q. Y. Yin, and H. L. Wei, "Spatiotemporal variations of residual stresses during multi-track and multi-layer deposition for laser powder bed fusion of Ti-6Al-4V," *Comput. Mater. Sci.*, vol. 195, Jul. 2021, Art. no. 110462.
[36] G. Z. Zeng, R. L. Zu, D. L. Wu, W. X. Shi, J. F. Zhou, J. Y. Zhao, Z. W. Liu, H. M. Xie, and S. Liu, "A hybrid method for the online evaluation of stress fields in metal additive manufacturing," *Experim. Mech.*, vol. 61, no. 8, pp. 1261–1270, Oct. 2021.
[37] T. Li, L. Zhang, G. Chen, N. Pirch, T. Schopphoven, A. Gasser, and R. Poprawe, "A combined heat source model for the prediction of residual stress post extreme high-speed laser material deposition," *J. Manuf. Processes*, vol. 78, pp. 265–277, Jun. 2022.
[38] D. Weisz-Patrault, P. Margerit, and A. Constantinescu, "Residual stresses in thin walled-structures manufactured by directed energy deposition: In-situ measurements, fast thermo-mechanical simulation and buckling," *Additive Manuf.*, vol. 56, Aug. 2022, Art. no. 102903.
[39] V. Nain, T. Engel, M. Carin, and D. Boisselier, "Conventional meso-scale and time-efficient sub-track-scale thermomechanical model for directed energy deposition," *Materials*, vol. 15, no. 12, p. 4093, Jun. 2022.

YUANXIN CHAI received the B.Eng. and M.Sc. degrees in mechanical engineering from the Liaoning University of Technology (LUT), Jinzhou, China, in 2017 and 2020, respectively. She is currently pursuing the Ph.D. degree in mechanical engineering with the Shenyang University of Technology (SUT), Shenyang, China. Her current research interests include additive manufacturing process optimization and process simulation, microstructure analysis, and residual stress characterization of metallic materials.

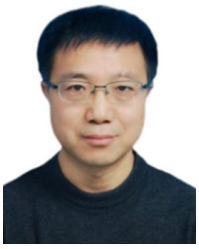

DIANQI LI received the M.Sc. degree in solid mechanics and the Ph.D. degree in pattern recognition and intelligent systems from Northeastern University (NEU), Shenyang, China, in 2002 and 2007, respectively. He is currently a Ph.D. Advisor with the Shenyang University of Technology (SUT), Shenyang. His current research interests include failure analysis and prediction of metallic materials under special service conditions, tissue modulation of metal matrix composites, and material preparation.

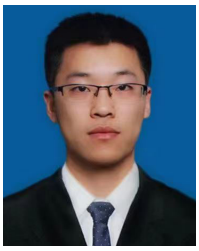

LIGUO MIAO received the B.Eng. and M.Sc. degrees in mechanical engineering from the Shenyang University of Technology (SUT), Shenyang, China, in 2016 and 2019, respectively, where he is currently pursuing the Ph.D. degree. His current research interests include additive manufacturing quality monitoring, microphysical characterization, and evaluation of metallic materials.

JINGHU TANG received the M.Sc. degree in mechanical engineering from the Shenyang University of Technology (SUT), Shenyang, China, in 2019. He is currently pursuing the Ph.D. degree in mechanical engineering with Northeastern University (NEU), Shenyang. His current research interests include process equipment design development, structure optimization, and precision machinery design and manufacturing.

FEI XING received the M.Sc. and Ph.D. degrees in mechatronic engineering from the Shenyang Institute of Automation, Chinese Academy of Sciences, Shenyang, China, in 2005 and 2009, respectively.

He is currently working with Nanjing Zhongke Raycham Laser Technology Company. His current research interests include modulation of tissue properties of high-temperature alloys and the special forming of refractory metal matrix composites. He has served as a member for the Academic Committee of the Chinese Society of Laser Processing and the Vice Chairperson for the China Additive Manufacturing Industry Alliance.